

First discovery of trans-iron elements in a DAO-type white dwarf (BD–22°3467)

L. Löbbling¹★, M. A. Maney^{1,2}, T. Rauch¹, P. Quinet^{3,4},
S. Gamrath³, J. W. Kruk⁵, and K. Werner¹

¹*Institute for Astronomy and Astrophysics, Kepler Center for Astro and Particle Physics, Eberhard Karls University, Sand 1, 72076 Tübingen, Germany*

²*Department of Astronomy & Astrophysics, Eberly College of Science, The Pennsylvania State University, 525 Davey Lab, University Park, PA 16802, USA*

³*Physique Atomique et Astrophysique, Université de Mons – UMONS, 7000 Mons, Belgium*

⁴*IPNAS, Université de Liège, Sart Tilman, 4000 Liège, Belgium*

⁵*NASA Goddard Space Flight Center, Greenbelt, MD 20771, USA*

Accepted 2019 November 18. Received 2019 November 11; in original form 2019 September 16

ABSTRACT

We have identified 484 lines of the trans-iron elements (TIEs) Zn, Ga, Ge, Se, Br, Kr, Sr, Zr, Mo, In, Te, I, Xe, and Ba, for the first time in the ultraviolet spectrum of a DAO-type WD, namely BD–22°3467, surrounded by the ionized nebula Abell 35. Our TIE abundance determination shows extremely high overabundances of up to five dex – a similar effect is already known from hot, H-deficient (DO-type) white dwarfs. In contrast to these where a pulse-driven convection zone has enriched the photosphere with TIEs during a final thermal pulse and radiative levitation has established the extreme TIE overabundances, here the extreme TIE overabundances are exclusively driven by radiative levitation on the initial stellar metallicity. The very low mass ($0.533^{+0.040}_{-0.025} M_{\odot}$) of BD–22°3467 implies that a third dredge-up with enrichment of s-process elements in the photosphere did not occur in the AGB precursor.

Key words: line: identification – planetary nebulae: individual: A66 35 – stars: abundances – stars: AGB and post-AGB – stars: atmospheres – stars: individual: BD–22°3467

1 INTRODUCTION

Trans-iron elements (TIEs) are synthesized during the asymptotic giant branch (AGB) phase of a star by the slow neutron-capture (s-)process. Depending on the initial stellar mass, its yields vary strongly (Karakas & Lugaro 2016). To become detectable, TIEs have to be transported from the helium-rich intershell region to the stellar surface. This happens, if the star experiences a third dredge-up (TDU, c.f., Herwig 2000). A scenario in which the envelope becomes mixed with the intershell region is known as the late helium-shell flash. Such a late thermal pulse (LTP) was predicted, e.g., by Iben et al. (1983). When it occurs after the star’s descent from the AGB at already declining luminosity, i.e., close to the end of nuclear burning, the H-burning shell is “off” and a pulse-driven convection zone (PDCZ) establishes between the He-burning shell and the photosphere. The remaining H is mixed into the stellar interior, becomes diluted or even burned, making

the star H-deficient (c.f., Fujimoto 1977; Schönberner 1979; Iben et al. 1983; Blöcker 1995). Thus, it was – although surprising – well understandable, that lines of ten TIEs were identified (Werner et al. 2012) in the ultraviolet (UV) spectrum of the DO-type white dwarf (WD) RE 0503–289 (effective temperature $T_{\text{eff}} = 70\,000 \pm 2000$ K, surface gravity $\log(g / \text{cm s}^{-2}) = 7.5 \pm 0.1$, Rauch et al. 2016b), which became an archetype for TIE search in WDs. Presently, 18 of these species are identified in RE 0503–289 (Rauch et al. submitted). Chayer et al. (2005) first succeeded in the detection of TIEs in DO WDs, namely six species in two other objects (HD 149499 B, HZ 21).

In a subsequent investigation, TIE line identification was successfully performed in three related H-deficient objects (two DO-type WDs and one PG 1159-type WD, namely WD 0111+002, PG 0109+111, and PG 1707+427, Hoyer et al. 2018). The commonality of these stars is that they are located close to the so-called PG 1159 wind limit (Unglaub & Bues 2000) that approximately separates the regions of PG 1159-type stars and DO-type WDs in the Hertzsprung-Russell diagram (HRD). Here, the stellar wind

★ E-mail: loebbling@astro.uni-tuebingen.de

is already weak enough and diffusion can establish strong TIE overabundances of up to five dex in the photosphere (Rauch et al. 2016a).

The search for TIE lines has not been restricted to He-rich WDs. Vennes et al. (2005) discovered the first TIE in WDs at all, namely Ge in three DA WDs. One of them is G191–B2B, an object that is employed as spectrophotometric flux standard for the Hubble Space Telescope (e.g., Bohlin 2007; Rauch et al. 2013). Recently, the TIEs Cu, Zn, Ga, Ge, As, Sn, and Ba were identified (Rauch et al. submitted, Rauch et al. 2014a, 2015, 2012, 2016a, 2013, 2014b). The TIE abundance pattern is similar to RE 0503–289, but at a lower absolute level probably because of the lower T_{eff} of G191–B2B ($T_{\text{eff}}=60\,000\text{ K}$, Rauch et al. 2013). TIE line search and abundance analyses are also successfully performed in the field of He-rich, hot subdwarf stars. The first one was LS IV–14°116, for which extreme overabundances of Fe, Sr, Y, and Zr were detected (Naslim et al. 2011). The most recent members of the group of “heavy metal” subdwarfs are HZ 44, HD 127493, and Feige 46 (e.g., Dorsch et al. 2019; Latour et al. 2019), with TIE enrichment patterns similar to those in Fig. 1.

Abell 35 was discovered by Abell (1955) and characterized as homogeneous disk planetary nebula (PN, Abell 1966). Jacoby (1981) classified the visible nucleus as G8 III–IV. Later, Grewing & Bianchi (1988) classified the hot, ionizing central star as DAO-type white dwarf (WD). Shortwards of 2800 \AA , the WD dominates the flux, whereas the cool companion outshines it in the optical. Herald & Bianchi (2002) analyzed the binary and found $T_{\text{eff}}=80\,000\text{ K}$ and $\log(g/\text{cm/s}^2) = 7.7$ for the hot and $T_{\text{eff}}=5\,000\text{ K}$ and $\log g=3.5$ for the cool star. Ziegler et al. (2012) corrected the surface gravity of the WD to $\log g=7.2$ and Frew & Parker (2010) classified the nebula as “bow shock nebula in a photoionized Strömgren sphere”. Recently, a close re-inspection of the UV spectrum of the exciting star of the ionized nebula Abell 35, BD–22°3467 (WD 1250-226, McCook & Sion 1999), led us to the identification of TIE absorption lines. In this work, a systematic TIE line search was performed in order to constrain abundances analogously to Hoyer et al. (2017, for RE 0503–289). It is based on the BD–22°3467 model of Ziegler et al. (2012, atmospheric parameters given in Table A1) that was calculated using the non-local thermodynamic equilibrium (NLTE) model-atmosphere code of the Tübingen NLTE Model Atmosphere Package (TMAP¹, Werner et al. 2003, 2012). In Sects. 2 and 3, we briefly describe the available observations and the model atmospheres used for the spectral analysis, respectively. In Sect. 4, the process of line identification and subsequent abundance measurement is explained. Lastly, we summarize our results and conclude in Sect. 5.

2 OBSERVATIONS

Our analysis is based on high-resolution Far Ultraviolet Spectroscopic Explorer (FUSE) and Space Telescope Imaging Spectrograph (HST/STIS) observations. These were obtained from the MAST² archive. The FUSE spectrum taken

with the LWRS aperture has a resolving power of $R = \lambda/\Delta\lambda \approx 20\,000$. Four STIS observations with grating E140M and $R = 45\,800$ are available. The observation log is shown in Table B1. We convolved the synthetic spectra with Gaussians to model the respective instrument’s resolution. The signal-to-noise ratio of the STIS observations was improved by co-adding the observations. The combined spectra are the same as used by Ziegler et al. (2012). No optical observation of the DAO WD are available, since the G-star companion dominates this spectral range.

3 MODEL ATMOSPHERES AND ATOMIC DATA

The analysis was carried out using TMAP. This code assumes plane-parallel geometry and calculates chemically homogeneous NLTE atmospheres in radiative and hydrostatic equilibrium.

For the TIEs Cu, Zn, Ga, Ge, Se, Br, Kr, Sr, Zr, Mo, In, Te, I, Xe, and Ba, we used the recently calculated data that is available via the Tübingen Oscillator Strengths Service (TOSS). For the elements with $Z \geq 20$, it is necessary to create model atoms using a statistical approach that calculates super levels and super lines (Rauch & Deetjen 2003) to take their complex atomic structure into account for the calculation. The statistics of all elements considered in our model-atmosphere calculations are summarized in Table B2.

We constructed a new classical model ion for Ba VIII from the level and line data of Churilov et al. (2001) available via the National Standards and Technology Institute (NIST) Atomic Spectra Database (ASD³, Kramida et al. 2018), which was incorporated into TMAD.

For all considered elements with an atomic number $Z \leq 28$, we used the same model atoms like Ziegler et al. (2012). For $Z < 20$ these were obtained from the Tübingen Model Atom Database (TMAD, Rauch & Deetjen 2003) that was constructed as part of the German Astrophysical Virtual Observatory (GAVO). For the iron-group elements (IGEs, atomic number $20 \leq Z \leq 28$), Kurucz’s line lists⁴ (Kurucz 2009, 2011, 2017) were utilized.

For this analysis, we adopted the photospheric parameters of Ziegler et al. (2012) and used their final model ($T_{\text{eff}}=80\,000\text{ K}$, $\log g=7.2$, see Table A1 for the element abundances) to start our TIE analysis. To identify lines and determine abundances of the 15 TIEs (Cu, Zn, Ga, Ge, Se, Br, Kr, Sr, Zr, Mo, In, Te, I, Xe, and Ba), we performed line-formation calculations by adding each of them individually to the start model from Ziegler et al. (2012), while temperature and density structure of the atmosphere were kept fixed. To verify our method, a final model including all TIEs with their previously determined abundances was then calculated with temperature and density corrections. The deviations in the abundances were marginal.

The observed spectra are affected by reddening due to interstellar material within the line of sight. By comparing the slope of the flux calibrated observations as well as GALEX, HIPPARCOS, and 2MASS magnitudes

¹ <http://astro.uni-tuebingen.de/~TMAP>

² <http://archive.stsci.edu>

³ <https://physics.nist.gov/PhysRefData/ASD>

⁴ <http://kurucz.harvard.edu/atoms.html>

(Bianchi et al. 2011; Perryman et al. 1997; Cutri et al. 2003) with the synthetic spectra of the central star, Ziegler et al. (2012) found a color excess $E_{B-V} = 0.02 \pm 0.02$. This value was used to apply interstellar reddening following the law of Fitzpatrick (1999, with the standard $R_V = 3.1$) to the model spectra to reproduce the observation. Absorption due to neutral interstellar hydrogen, assuming a column density of $N_{\text{H I}} = 5.0 \times 10^{20} \text{ cm}^{-2}$ (Ziegler et al. 2012), was applied to the synthetic spectra. Furthermore, we applied the interstellar line-absorption model of Ziegler et al. (2012) that was calculated using the program OWENS (Hébrard et al. 2002; Hébrard & Moos 2003) to unambiguously identify lines of stellar and interstellar origin.

4 LINE IDENTIFICATION AND ABUNDANCE DETERMINATION

We calculated synthetic spectra from our line-formation models with each of the 15 elements added individually to the best model of Ziegler et al. (2012). The spectrum is crowded with a multitude of blended metal lines which hampers their unambiguous identification. To clearly see the contribution of the individual TIE elements, we divided the synthetic spectrum including this species by another model spectrum without it. The individual abundances were varied by small steps of 0.2 dex or smaller to derive the final values from evaluation of line-profile fits by eye. To estimate the influence of the uncertainty in T_{eff} of $\pm 10\,000 \text{ K}$ and in $\log g$ of ± 0.3 for the error propagation, we redid the abundance determination for models with $T_{\text{eff}} = 90\,000 \text{ K}$ and $\log g = 6.9$ as well as for $T_{\text{eff}} = 70\,000 \text{ K}$ and $\log g = 7.5$. The abundances are affected by typical errors below 0.3 dex.

For Cu, a line identification was not possible with appreciable certainty. Instead, upper limits were determined by reducing the abundance until the strongest computed lines become undetectable. An equivalent width of $W_\lambda = 5 \text{ mÅ}$ was set as a detection limit. Table B3 – Table B17 list all lines of TIEs, that appear with an equivalent width above the threshold in the model spectrum. These tables include also those lines that could not be identified in the spectrum of BD-22°3467 due to, e.g., blending with other photospheric or interstellar lines to make them a useful tool for the identification of TIE lines in the spectra of other DAO-type WDs. The abundances are given in Table A1 and are illustrated in Fig. 1. The complete FUSE and STIS observations compared to our best model are shown online⁵ within the Tübingen Visualization tool (TVIS). The ionization fractions as well as the temperature structure and electron density in the final atmosphere model are shown in Fig. B1.

The number of identified lines per TIE ion is shown in Table 1. The observation is well reproduced by our final model with the abundances shown in Table A1 as it is illustrated in Fig. B2 to B16 for prominent lines of each of the TIEs.

Table 1. Numbers of identified lines in the ionization stages IV–VIII of TIEs in the UV spectrum of BD-22°3467.

Element	Z	IV	V	VI	VII	VIII
Zn	30	2	141			
Ga	31	2	71	52		
Ge	32	2	32	57		
Se	34		14			
Br	35		1	7		
Kr	36			4		
Sr	38		17			
Zr	40		1	28	3	
Mo	42			2		
In	49		28			
Te	52			3		
I	53			4		
Xe	54				4	
Ba	56				3	3

5 RESULTS AND CONCLUSIONS

To identify TIE lines, the UV spectrum of BD-22°3467 was closely inspected which led to the discovery of Zn, Ga, Ge, Se, Br, Kr, Sr, Zr, Mo, In, Te, I, Xe, and Ba (Table 1). In total, 484 TIE lines were discovered.

Our spectral analysis has shown that the enrichment of TIEs in BD-22°3467 ($T_{\text{eff}} = 80\,000 \pm 10\,000 \text{ K}$, $\log g = 7.2 \pm 0.3$) and RE 0503-289 ($T_{\text{eff}} = 70\,000 \pm 2000 \text{ K}$, $\log g = 7.5 \pm 0.1$) is comparably high ($\approx 1.5 - 5 \text{ dex}$, Fig. 1). The origin of the high enrichment of TIEs is diffusion, i.e., efficient radiative levitation. This was shown already for RE 0503-289 by detailed diffusion calculations (Rauch et al. 2016a). While it was possible to determine abundances for several TIEs with consecutive atomic number in RE 0503-289 and find that the odd-even shape of the solar abundance pattern seems to be reflected also by the enriched TIEs (Fig. 2, cf., Rauch et al. 2019, submitted), there is not enough information to confirm this finding based on the results for BD-22°3467.

The evolutionary difference between BD-22°3467 and RE 0503-289 is that the latter most likely experienced an LTP in which it became hydrogen-deficient. As a result, a pulse-driven convection zone, established during the flash, enriched the TIEs in the atmosphere. Their abundances were later on amplified to the observed values by radiative levitation. In contrast, the high abundances of TIEs in BD-22°3467 are possibly the result of radiative levitation on the initial stellar metallicity without previous enrichment by s-processed matter. This is because of the very low mass of BD-22°3467, (Fig. 1) which corresponds to an initial mass of below $1.0 M_\odot$ (Cummings et al. 2018), implying that no TDU occurred on the AGB (Karakas & Lugaro 2016). From the position in the $T_{\text{eff}} - \log g$ diagram (Fig. 3) only, a possible evolution without an AGB phase, directly from the extended horizontal branch (EHB) to the WD cooling sequence, cannot be excluded. Conversely, it is then possible that the high amount of TIEs in RE 0503-289 is solely due to diffusion, independent of the occurrence of a previous LTP. This is an interesting conclusion, because a large fraction of DOs is not initiated by an LTP but by a merger event with the so-called O(He) stars as merger products and DO precursors (Reindl et al. 2014). DOs from this evolutionary chan-

⁵ <http://astro.uni-tuebingen.de/~TVIS/objects/Abell135>

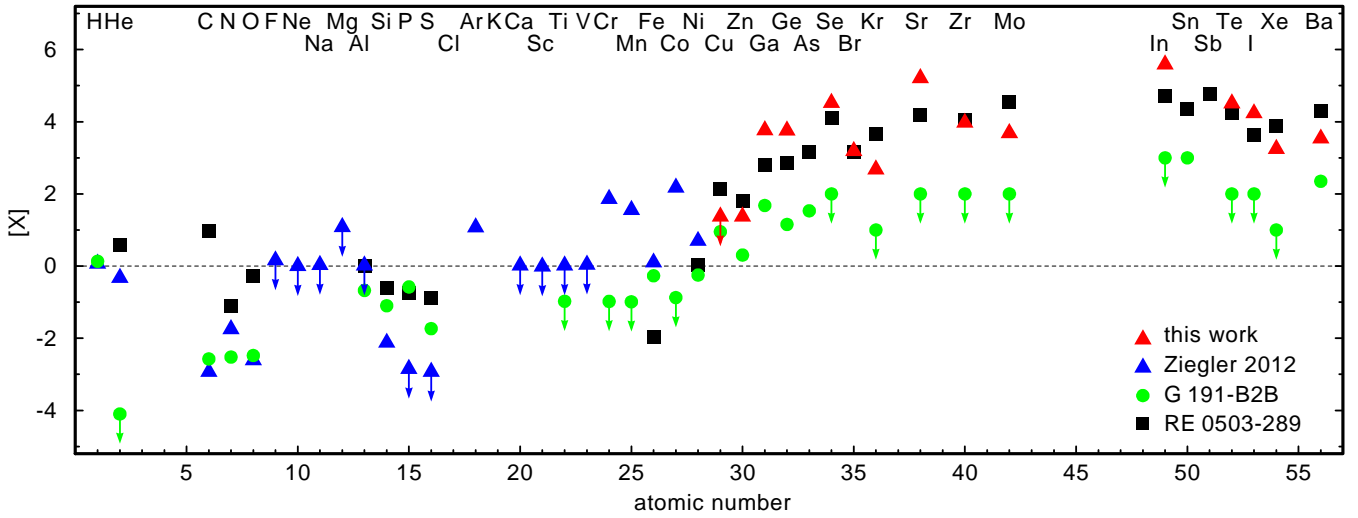


Figure 1. Photospheric abundance ratios $[X] = \log(\text{mass fraction}/\text{solar mass fraction})$ of BD-22°3467 determined from detailed line profile fits. Solar values are taken from [Asplund et al. \(2009\)](#); [Scott et al. \(2015b,a\)](#); [Grevesse et al. \(2015\)](#). Upper limits are indicated with arrows. The black, solid line indicates solar abundances. Blue triangles represent the abundances determined by [Ziegler et al. \(2012\)](#), red triangles show the TIE abundances (Table A1). For comparison, the abundances determined for G191-B2B ([Rauch et al. 2013](#), green circles) and RE0503-289 are shown ([Hoyer et al. 2017](#), black squares).

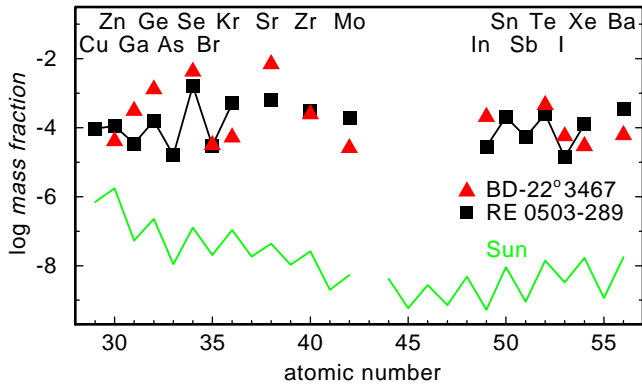


Figure 2. Photospheric TIE abundances in BD-22°3467 (red triangles) compared to RE0503-289 (black squares [Hoyer et al. 2017](#), [Rauch et al. 2019 submitted](#)). Solar values are shown for comparison.

nel should therefore also go through a phase with an extreme TIE enrichment by diffusion.

We have to keep in mind that diffusion-established abundance patterns do not contain anymore information about the previous stellar evolution, i.e., wherever the TIEs (or other elements) stem from, the exhibited surface abundance may be the same. Investigations on yields of the AGB s-process nucleosynthesis elements have to be performed before diffusion dominates the stellar evolution. This is the phase of just declining luminosity when the strength of the stellar wind decreases but is still high enough to maintain the original abundance ratios produced by the s-process. Spectral analyses of stars in that evolutionary phase might help to directly constrain AGB nucleosynthesis.

The formation of Abell 35-like central stars of planetary nebulae (CSPNe), i.e., binary CSPNe with a rapidly rotating late-type (sub)giant and an extremely hot companion

([Bond et al. 1993](#)), is discussed controversially in the literature. [Thevenin & Jasniewicz \(1997\)](#) found the companion of BD-22°3467 to be enriched in Ba indicating that this still unevolved star experienced mass transfer from a (post-) AGB star. However, this formation channel is debated since Abell 35 was found to only mimic a PN ([Frew & Parker 2010](#)) and the mass of the ionizing star was considered to be too low for a post-AGB star ([Ziegler et al. 2012](#)). As explained above, an evolution directly from the EHB to the WD cooling track is possible (Fig. 3). The peculiar ionized nebula around BD-22°3467 is not a real PN but, nevertheless, it also cannot be excluded, that the nebula material is in some way connected to the evolution of the central star. Assuming that it ejected a PN as an AGB star, the original PN might have already dispersed. The star has a high proper motion ($\mu_\alpha = -54.566 \pm 0.226$ mas/yr and $\mu_\delta = -10.097 \pm 0.187$ mas/yr, [Gaia Collaboration et al. 2018](#)) and, thus, might now be passing through the edges of the ejected former nebula material or another dense ISM region while ionizing the surrounding material. The classification of Abell 35 as a bow shock nebula in a photoionized Strömgen sphere in the ambient ISM ([Frew & Parker 2010](#)) does not necessarily include a PN but also, does not rule out the post-AGB nature of BD-22°3467. Further detailed abundance analyses of a sample of Abell 35-like CSPNe as well as their ambient nebulae and companion stars should give us a better handle on their evolution. The nebulae, if ejected from an AGB star, contain signatures of s-process elements ([Madonna et al. 2017](#)) as well as the unevolved companions, if they accreted a fraction of the ejected material. Therefore, a precise knowledge of the companion is mandatory because any accreted material would become diluted in this star's convective envelope.

To better understand the late evolutionary phases of low-mass stars, it is highly desirable to improve the determination of T_{eff} and $\log g$ with much narrower error ranges. For

this purpose, the analysis of high-resolution optical spectra, may be helpful. Although the cool companion dominates this wavelength regime, broad lines of H and He of BD-22°3467 should be detectable like demonstrated by [Aller et al. \(2015\)](#) for the binary CS of NGC 1514. These lines may reduce the error and, thus, allow to better constrain the stellar mass (Fig. 3).

As a remark, we would like to mention that the discrepancy found by [Ziegler et al. \(2012\)](#) between the spectroscopic distance of 361_{-137}^{+195} pc and the distance based on the HIPPARCOS parallax is still present in the era of Gaia with a distance of $124.84_{-2.13}^{+2.21}$ pc ([Bailer-Jones et al. 2018](#)). [Ziegler et al. \(2012\)](#) demonstrated, that the H I lines in the FUSE range are poorly reproduced with models with $\log g > 7.7$. This phenomenon of too large spectroscopic distances has already been reported in the literature for CSPNe ([Schönberner et al. 2018](#); [Schönberner & Steffen 2019](#)). The argument that missing metal-line blanketing and back warming may result in too-high temperatures does not hold in our analysis, because all elements in the model calculation were considered in full NLTE computations. The objects of the mentioned studies are all located before the knee at highest temperatures in the Hertzsprung-Russell diagram. Thus, the spectroscopic mass derived from fitting of the spectral energy distribution using the parallax distance is systematically too high. In our case, the spectroscopic mass derived from the dereddened GALEX FUV flux ([Bianchi et al. 2011](#)) using the Gaia distance is unreasonably low. With the given T_{eff} , at least a $\log g > 8.0$ would be required to reach masses above $0.4 M_{\odot}$. In conclusion, the discrepancy remains unexplained and needs further investigation.

Following the discovery of TIE lines in BD-22°3467, we have initiated an analogous search in other DAO-type WDs. Since the FUSE and HST archives provide quite a number of high-quality UV spectra of such stars, that have not been inspected in focus of TIEs, we expect to identify TIE enrichment as a common phenomenon in many hot WDs.

ACKNOWLEDGMENTS

We thank the referee for the very useful comments that improved this paper. LL has been supported by the German Research Foundation (DFG) under grant WE 1312/49-1. MAM had been supported by the DAAD RISE Germany program. The GAVO project at Tübingen had been supported by the Federal Ministry of Education and Research (BMBF) at Tübingen (05 AC 6 VTB, 05 AC 11 VTB). Financial support from the Belgian FRS-FNRS is also acknowledged. PQ is research director of this organization. Some of the data presented in this paper were obtained from the Mikulski Archive for Space Telescopes (MAST). STScI is operated by the Association of Universities for Research in Astronomy, Inc., under NASA contract NAS5-26555. Support for MAST for non-HST data is provided by the NASA Office of Space Science via grant NNX09AF08G and by other grants and contracts. The TIRO (<http://astro-uni-tuebingen.de/~TIRO>), TMAD (<http://astro-uni-tuebingen.de/~TMAD>), TOSS (<http://astro-uni-tuebingen.de/~TOSS>), and TVIS (<http://astro-uni-tuebingen.de/~TVIS>) tools and ser-

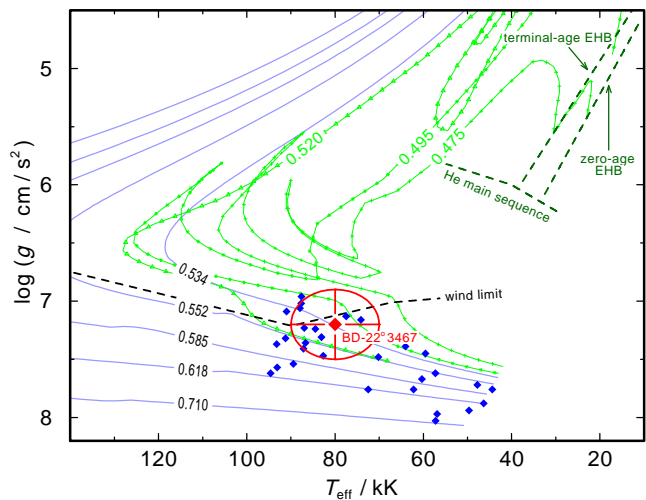


Figure 3. Location of BD-22°3467 (green) with error ellipse in the T_{eff} - $\log g$ diagram compared to other DAO-type WDs ([Gianninas et al. 2010](#), blue diamonds). Included are post-EHB evolutionary tracks (green, [Dorman et al. 1993, \$Y = 0.288 \approx Y_{\odot}\$ \) and post-AGB tracks for H-burners \(blue, \[Miller Bertolami 2016\]\(#\)\) labeled with the stellar mass \(in \$M_{\odot}\$ \). The wind limit for H-rich post-AGB stars is indicated \(\[Ungraub & Bues 2000\]\(#\)\).](#)

vices used for this paper were constructed as part of the Tübingen project (<https://uni-tuebingen.de/de/122430>) of the German Astrophysical Virtual Observatory (GAVO, <http://www.g-vo.org>). This research has made use of NASA’s Astrophysics Data System and of the SIMBAD database, operated at CDS, Strasbourg, France. This work has made use of data from the European Space Agency (ESA) mission *Gaia* (<https://www.cosmos.esa.int/gaia>), processed by the *Gaia* Data Processing and Analysis Consortium (DPAC, <https://www.cosmos.esa.int/web/gaia/dpac/consortium>). Funding for the DPAC has been provided by national institutions, in particular the institutions participating in the *Gaia* Multilateral Agreement.

References

- Abell G. O., 1955, *PASP*, 67, 258
- Abell G. O., 1966, *ApJ*, 144, 259
- Aller A., Miranda L. F., Olguín L., Vázquez R., Guillén P. F., Oreiro R., Ulla A., Solano E., 2015, *MNRAS*, 446, 317
- Asplund M., Grevesse N., Sauval A. J., Scott P., 2009, *ARA&A*, 47, 481
- Bailer-Jones C. A. L., Rybizki J., Fouesneau M., Mantelet G., Andrae R., 2018, *AJ*, 156, 58
- Bianchi L., Herald J., Efremova B., Girardi L., Zobot A., Marigo P., Conti A., Shiao B., 2011, *Ap&SS*, 335, 161
- Blöcker T., 1995, *A&A*, 299, 755
- Bohlin R. C., 2007, in *Astronomical Society of the Pacific Conference Series*, Vol. 364, Sterken C., ed, *The Future of Photometric, Spectrophotometric and Polarimetric Standardization*, p. 315
- Bond H. E., Ciardullo R., Meakes M. G., 1993, in *IAU Symposium*, Vol. 155, Weinberger R., Acker A., ed, *Planetary Nebulae*, p. 397

- Chayer P., Vennes S., Dupuis J., Kruk J. W., 2005, *ApJ*, 630, L169
- Churilov S. S., Joshi Y. N., Gayasov R., 2001, *J. Opt. Soc. Am. B*, 18, 113
- Cummings J. D., Kalirai J. S., Tremblay P.-E., Ramirez-Ruiz E., Choi J., 2018, *ApJ*, 866, 21
- Cutri R. M. et al., 2003, 2MASS All Sky Catalog of point sources.
- Dorman B., Rood R. T., O'Connell R. W., 1993, *ApJ*, 419, 596
- Dorsch M., Latour M., Heber U., 2019, *A&A*, 630, A130
- Fitzpatrick E. L., 1999, *PASP*, 111, 63
- Frew D. J., Parker Q. A., 2010, *Publ. Astron. Soc. Australia*, 27, 129
- Fujimoto M. Y., 1977, *PASJ*, 29, 331
- Gaia Collaboration et al., 2018, *A&A*, 616, A1
- Gianninas A., Bergeron P., Dupuis J., Ruiz M. T., 2010, *ApJ*, 720, 581
- Grevesse N., Scott P., Asplund M., Sauval A. J., 2015, *A&A*, 573, A27
- Grewing M., Bianchi L., 1988, in *ESA Special Publication*, Vol. 2, p. 177
- Hébrard G. et al., 2002, *Planet. Space Sci.*, 50, 1169
- Hébrard G., Moos H. W., 2003, *ApJ*, 599, 297
- Herald J. E., Bianchi L., 2002, *ApJ*, 580, 434
- Herwig F., 2000, *A&A*, 360, 952
- Hoyer D., Rauch T., Werner K., Kruk J. W., 2018, *A&A*, 612, A62
- Hoyer D., Rauch T., Werner K., Kruk J. W., Quinet P., 2017, *A&A*, 598, A135
- Iben I., Jr., Kaler J. B., Truran J. W., Renzini A., 1983, *ApJ*, 264, 605
- Jacoby G. H., 1981, *ApJ*, 244, 903
- Karakas A. I., Lugaro M., 2016, *ApJ*, 825, 26
- Kramida A., Yu. Ralchenko, Reader J., NIST ASD Team, 2018, NIST Atomic Spectra Database (ver. 5.6.1), [Online]. Available: <https://physics.nist.gov/asd> [2017, April 9]. National Institute of Standards and Technology, Gaithersburg, MD.
- Kurucz R. L., 2009, in *American Institute of Physics Conference Series*, Vol. 1171, Hubeny I., Stone J. M., MacGregor K., Werner K., ed, American Institute of Physics Conference Series, p. 43
- Kurucz R. L., 2011, *Canadian Journal of Physics*, 89, 417
- Kurucz R. L., 2017, *Canadian Journal of Physics*, 95, 825
- Latour M., Dorsch M., Heber U., 2019, *A&A*, 629, A148
- Madonna S., García-Rojas J., Sterling N. C., Delgado-Inglada G., Mesa-Delgado A., Luridiana V., Röderer I. U., Mashburn A. L., 2017, *MNRAS*, 471, 1341
- McCook G. P., Sion E. M., 1999, *ApJS*, 121, 1
- Miller Bertolami M. M., 2016, *A&A*, 588, A25
- Naslim N., Jeffery C. S., Behara N. T., Hibbert A., 2011, *MNRAS*, 412, 363
- Perryman M. A. C. et al., 1997, *A&A*, 500, 501
- Rauch T., Deetjen J. L., 2003, in *Astronomical Society of the Pacific Conference Series*, Vol. 288, Hubeny I., Mihalas D., Werner K., ed, *Stellar Atmosphere Modeling*, p. 103
- Rauch T., Quinet P., Hoyer D., Werner K., Demleitner M., Kruk J. W., 2016a, *A&A*, 587, A39
- Rauch T., Quinet P., Hoyer D., Werner K., Richter P., Kruk J. W., Demleitner M., 2016b, *A&A*, 590, A128
- Rauch T., Werner K., Biéumont É., Quinet P., Kruk J. W., 2012, *A&A*, 546, A55
- Rauch T., Werner K., Bohlin R., Kruk J. W., 2013, *A&A*, 560, A106
- Rauch T., Werner K., Quinet P., Kruk J. W., 2014a, *A&A*, 564, A41
- Rauch T., Werner K., Quinet P., Kruk J. W., 2014b, *A&A*, 566, A10
- Rauch T., Werner K., Quinet P., Kruk J. W., 2015, *A&A*, 577, A6
- Reindl N., Rauch T., Werner K., Kepler S. O., Gänsicke B. T., Gentile Fusillo N. P., 2014, *A&A*, 572, A117
- Schönberner D., 1979, *A&A*, 79, 108
- Schönberner D., Balick B., Jacob R., 2018, *A&A*, 609, A126
- Schönberner D., Steffen M., 2019, *A&A*, 625, A137
- Scott P., Asplund M., Grevesse N., Bergemann M., Sauval A. J., 2015a, *A&A*, 573, A26
- Scott P. et al., 2015b, *A&A*, 573, A25
- Thevenin F., Jasniewicz G., 1997, *A&A*, 320, 913
- Unglaub K., Bues I., 2000, *A&A*, 359, 1042
- Vennes S., Chayer P., Dupuis J., 2005, *ApJ*, 622, L121
- Werner K., Deetjen J. L., Dreizler S., Nagel T., Rauch T., Schuh S. L., 2003, in *Astronomical Society of the Pacific Conference Series*, Vol. 288, Hubeny I., Mihalas D., Werner K., ed, *Stellar Atmosphere Modeling*, p. 31
- Werner K., Dreizler S., Rauch T., 2012, TMAP: Tübingen NLTE Model-Atmosphere Package, Astrophysics Source Code Library
- Werner K., Rauch T., Ringat E., Kruk J. W., 2012, *ApJ*, 753, L7
- Ziegler M., Rauch T., Werner K., Köppen J., Kruk J. W., 2012, *A&A*, 548, A109

**APPENDIX A: PHOTOSPHERIC
PARAMETERS OF BD-22°3467**

Table A1. Parameters of BD–22°3467.

$T_{\text{eff}} / \text{K}$	$80\,000 \pm 10\,000^{(a)}$				
$\log(g / \text{cm/s}^2)$	$7.2 \pm 0.3^{(a)}$				
E_{B-V}	$0.02 \pm 0.02^{(a)}$				
$\log N_{\text{H I}} / \text{cm}^{-2}$	$20.7 \pm 0.1^{(a)}$				
M / M_{\odot}	$0.533^{+0.040}_{-0.025}^{(b)}$	$0.505^{+0.030}_{-0.025}^{(c)}$			
$\log(L / L_{\odot})$	$1.52^{+0.40}_{-0.50}^{(b)}$	$1.69^{+0.30}_{-0.50}^{(c)}$			
Element	[X]	Mass fraction	Number fraction	$\epsilon^{(d)}$	[X/Fe]
H ^(a)	0.07	8.67×10^{-1}	9.67×10^{-1}	12.09	–0.00
He ^(a)	–0.33	1.17×10^{-1}	3.29×10^{-2}	10.62	–0.40
C ^(a)	–2.93	2.77×10^{-6}	2.59×10^{-7}	5.51	–3.00
N ^(a)	–1.75	1.24×10^{-5}	9.99×10^{-7}	6.10	–1.82
O ^(a)	–2.61	1.42×10^{-5}	9.99×10^{-7}	6.10	–2.68
F ^(a)	≤ 0.16	$\leq 5.04 \times 10^{-7}$	$\leq 2.98 \times 10^{-8}$	≤ 4.57	≤ -0.07
Ne ^(a)	≤ -0.00	$\leq 1.26 \times 10^{-3}$	$\leq 6.99 \times 10^{-5}$	≤ 7.94	≤ -0.07
Na ^(a)	≤ 0.03	$\leq 2.92 \times 10^{-5}$	$\leq 1.43 \times 10^{-6}$	≤ 6.25	≤ -0.07
Mg ^(a)	≤ 1.08	$\leq 8.31 \times 10^{-3}$	$\leq 3.84 \times 10^{-4}$	≤ 8.68	≤ 1.00
Al ^(a)	≤ 0.02	$\leq 5.56 \times 10^{-5}$	$\leq 2.31 \times 10^{-6}$	≤ 6.46	≤ -0.07
Si ^(a)	–2.12	5.00×10^{-6}	2.00×10^{-7}	5.40	–2.19
P ^(a)	≤ -2.85	$\leq 8.26 \times 10^{-9}$	$\leq 3.00 \times 10^{-10}$	≤ 2.58	≤ -2.92
S ^(a)	≤ -2.93	$\leq 3.64 \times 10^{-7}$	$\leq 1.27 \times 10^{-8}$	≤ 4.21	≤ -3.00
Ar ^(a)	1.07	8.65×10^{-4}	2.43×10^{-5}	7.49	1.00
Ca ^(a)	≤ 0.02	$\leq 6.41 \times 10^{-5}$	$\leq 1.80 \times 10^{-6}$	≤ 6.35	≤ -0.07
Sc ^(a)	≤ -0.01	$\leq 4.64 \times 10^{-8}$	$\leq 1.16 \times 10^{-9}$	≤ 3.16	≤ -0.07
Ti ^(a)	≤ 0.02	$\leq 3.12 \times 10^{-6}$	$\leq 7.31 \times 10^{-8}$	≤ 4.96	≤ -0.07
V ^(a)	≤ 0.04	$\leq 3.17 \times 10^{-7}$	$\leq 6.99 \times 10^{-9}$	≤ 3.94	≤ -0.07
Cr ^(a)	1.86	1.16×10^{-3}	2.50×10^{-5}	7.50	1.77
Mn ^(a)	1.56	3.81×10^{-4}	7.80×10^{-6}	6.99	1.48
Fe ^(a)	0.10	1.52×10^{-3}	3.06×10^{-5}	7.58	0.00
Co ^(a)	2.18	1.57×10^{-4}	3.00×10^{-6}	6.58	1.50
Ni ^(a)	0.70	3.39×10^{-4}	6.49×10^{-6}	6.91	0.61
Cu	≤ 1.38	$\leq 1.70 \times 10^{-5}$	$\leq 3.00 \times 10^{-7}$	≤ 5.58	≤ 1.30
Zn	1.37	4.08×10^{-5}	7.00×10^{-7}	5.95	1.30
Ga	3.77	3.11×10^{-4}	5.00×10^{-6}	6.80	3.67
Ge	3.76	1.29×10^{-3}	2.00×10^{-5}	7.40	3.67
Se	4.52	4.21×10^{-3}	6.00×10^{-5}	7.88	4.45
Br	3.19	3.13×10^{-5}	4.40×10^{-7}	5.74	3.12
Kr	2.68	5.23×10^{-5}	7.00×10^{-7}	5.95	2.61
Sr	5.21	6.98×10^{-3}	9.00×10^{-5}	8.05	5.10
Zr	3.97	2.44×10^{-4}	3.00×10^{-6}	6.58	3.91
Mo	3.68	2.57×10^{-5}	3.00×10^{-7}	5.58	3.61
In	5.83	3.58×10^{-4}	3.50×10^{-6}	6.64	5.76
Te	4.51	4.55×10^{-4}	4.00×10^{-6}	6.70	4.44
I	4.24	5.66×10^{-5}	5.00×10^{-7}	5.80	4.16
Xe	3.85	1.17×10^{-4}	1.00×10^{-6}	6.10	3.77
Ba	3.54	6.12×10^{-5}	5.00×10^{-7}	5.80	3.53

Notes. ^(a)From Ziegler et al. (2012). ^(b)Interpolated from post-AGB evolutionary tracks, cf., Fig. 3. ^(c)Interpolated from post-EHB evolutionary tracks, cf., Fig. 3. ^(d)Abundances $\epsilon_i = \log n_i + c$ with $\sum_i a_i n_i = 12.15$ and the atomic weights a_i .

APPENDIX B: ADDITIONAL FIGURES AND TABLES.

Table B1. Observation log for BD-22°3467.

Instrument	Dataset Id	Start Time (UT)	Wavelength range (λ)	Aperture/Grating	Exposure time (s)	Resolving power $R = \lambda / \Delta\lambda$
FUSE ^a	P1330101000	2000-05-20 20:27:37	910 – 1180	LWRS	4416	20 000
STIS ^b	O4GT02010	1999-04-17 21:14:49	1150 – 1730	E140M	2050	45 800
STIS	O4GT02020	1999-04-17 22:37:03	1150 – 1730	E140M	2800	45 800
STIS	O4GT02030	1999-04-18 00:16:10	1150 – 1730	E140M	2740	45 800
STIS	O4GT02040	1999-04-18 01:52:54	1150 – 1730	E140M	2740	45 800

Notes. a: Far Ultraviolet Spectroscopic Explorer, b: Space Telescope Imaging Spectrograph.

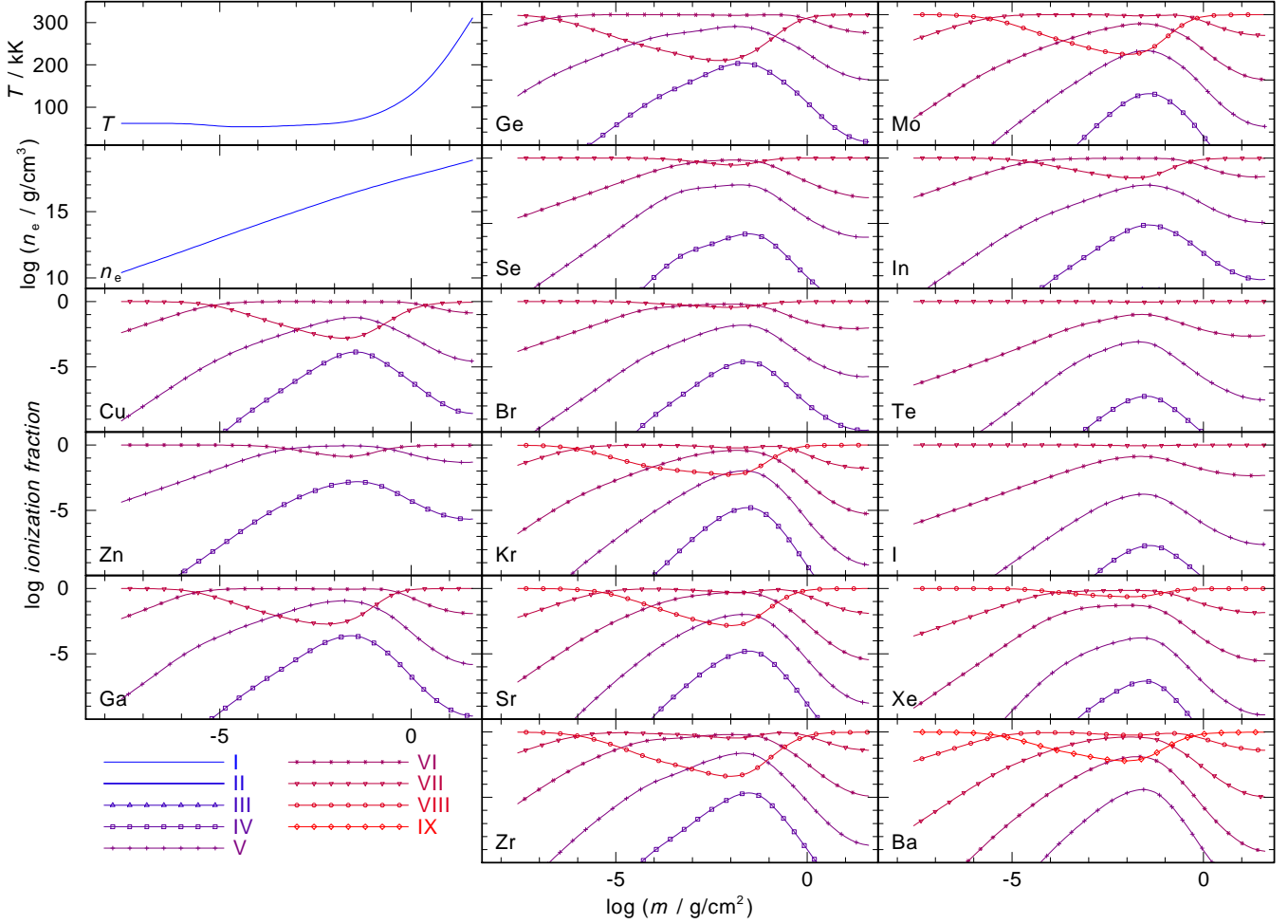


Figure B1. Temperature and electron density structure and ionization fractions of all TIE ions which are considered in our final model for BD-22°3467.

Table B2. Statistics of the H – Ar^a and Ca - Ba^b model atoms used in our model-atmosphere calculations.

Ion	Levels		Lines	Ion	Super levels ^c	Super lines	Individual lines	Ion	Super levels ^c	Super lines	Individual lines
	NLTE	LTE									
H I	12	4	66	Ca IV	6	16	20291	Cu IV	7	15	8785
H II	1	–	–	Ca V	6	21	141956	Cu V	7	16	5456
He I	5	98	3	Ca VI	6	19	114545	Cu VI	7	9	3797
He II	16	16	120	Ca VII	6	21	71608	Cu VII	1	0	0
C III	1	–	–	Ca VIII	6	20	9124	Zn IV	7	11	400
C IV	6	61	12	Ca IX	1	0	0	Zn V	7	15	1879
C V	54	4	295	Sc IV	6	20	15024	Zn VI	1	0	0
C VI	1	0	0	Sc V	6	21	261235	Ga IV	7	19	3198
N III	1	65	0	Sc VI	6	19	237271	Ga V	7	15	517
N IV	16	78	30	Sc VII	6	20	176143	Ga VI	7	13	1914
N V	54	8	297	Sc VIII	6	21	91935	Ga VII	1	0	0
N VI	1	0	0	Sc IX	1	0	0	Ge IV ^d	8	0	8
O III	3	69	0	Ti IV	6	19	1000	Ge V	7	16	2159
O IV	18	76	39	Ti V	6	20	26654	Ge VI	7	12	414
O V	90	36	610	Ti VI	6	19	95448	Ge VII	1	0	0
O VI	54	8	291	Ti VII	6	20	230618	Se IV	1	0	0
O VII	1	0	0	Ti VIII	6	21	182699	Se V	7	19	310
F III	1	6	0	Ti IX	1	0	0	Se VI	1	0	0
F IV	1	10	0	V IV	6	19	37130	Se VII	1	0	0
F V	15	91	31	V V	6	20	2123	Br III	1	0	0
F VI	12	115	16	V VI	6	19	35251	Br IV	6	12	424
F VII	1	0	0	V VII	6	19	112883	Br V	7	18	394
Ne II	1	33	0	V VIII	6	20	345089	Br VI	7	17	158
Ne III	3	43	0	V IX	1	0	0	Br VII	1	0	0
Ne IV	3	37	0	Cr IV	6	20	234170	Kr IV	7	19	911
Ne V	20	74	35	Cr V	6	20	43860	Kr V	7	16	553
Ne VI	1	0	0	Cr VI	6	20	4406	Kr VI	7	19	843
Na III	1	186	0	Cr VII	6	19	37070	Kr VII	7	21	743
Na IV	1	237	0	Cr VIII	6	20	132221	Kr VIII	1	0	0
Na V	8	42	9	Cr IX	1	0	0	Sr IV	7	21	7578
Na VI	43	10	130	Mn IV	6	20	719387	Sr V	7	19	2022
Na VII	1	0	0	Mn V	6	20	285376	Sr VI	7	10	70
Mg III	1	34	0	Mn VI	6	20	70116	Sr VII	7	10	46
Mg IV	31	0	93	Mn VII	6	20	8277	Sr VIII	1	0	0
Mg V	15	37	18	Mn VIII	6	20	37168	Zr IV	7	20	135
Mg VI	1	0	0	Mn IX	1	0	0	Zr V	7	22	1449
Al III	1	6	0	Fe IV	6	20	3102371	Zr VI	7	12	1098
Al IV	15	2	0	Fe V	6	20	3266247	Zr VII	7	15	947
Al V	1	16	0	Fe VI	6	20	991935	Zr VIII	1	0	0
Al VI	14	24	16	Fe VII	6	20	200455	Mo IV	7	15	2803
Al VII	1	0	0	Fe VIII	6	18	19587	Mo V	7	22	5829
Si III	3	31	1	Fe IX	1	0	0	Mo VI	7	23	984
Si IV	16	7	44	Co IV	6	20	552916	Mo VII	7	16	1173
Si V	25	0	59	Co V	6	20	1469717	Mo VIII	1	0	0
Si VI	1	0	0	Co VI	6	18	898484	In III	1	0	0
P III	1	9	0	Co VII	6	19	492913	In IV	7	14	564
P IV	15	36	9	Co VIII	6	20	88548	In V	7	10	919
P V	18	7	12	Co IX	1	0	0	In VI	8	10	176
P VI	1	0	0	Ni IV	6	20	2512561	In VII	1	0	0
S III	6	94	4	Ni V	6	20	2766664	Te IV	1	0	0
S IV	21	89	37	Ni VI	6	18	7408657	Te V	1	0	0
S V	18	19	48	Ni VII	6	18	4195381	Te VI	7	12	178
S VI	1	0	0	Ni VIII	6	20	1473122	Te VII	1	0	0
Ar IV	1	349	0	Ni IX	1	0	0	I IV	1	0	0
Ar V	32	329	38					I V	1	0	0
Ar VI	16	168	21					I VI	7	15	197
Ar VII	40	112	130					I VII	1	0	0
Ar VIII	1	0	0					I VIII	1	0	0
								I IX	1	0	0
								Xe IV	7	16	1391
								Xe V	7	15	616
								Xe VI	7	16	243
								Xe VII	7	19	491
								Xe VIII	1	0	0
								Ba V	7	12	981
								Ba VI	7	6	162
								Ba VII	7	11	493
								Ba VIII ^e	34	0	44
								Ba IX	1	0	0
total	742	2776	2514		279	884	33219636		359	651	63444

Notes. ^(a)classical model atoms, ^(b)model atoms constructed using a statistical approach (Rauch & Deetjen 2003), ^(c)treated as NLTE levels, ^(d)Ge IV classical model atom with 8 NLTE levels, 1 LTE level, and 8 transitions, ^(e)Ba VIII classical model atom with 34 NLTE levels, 0 LTE level, and 44 transitions.

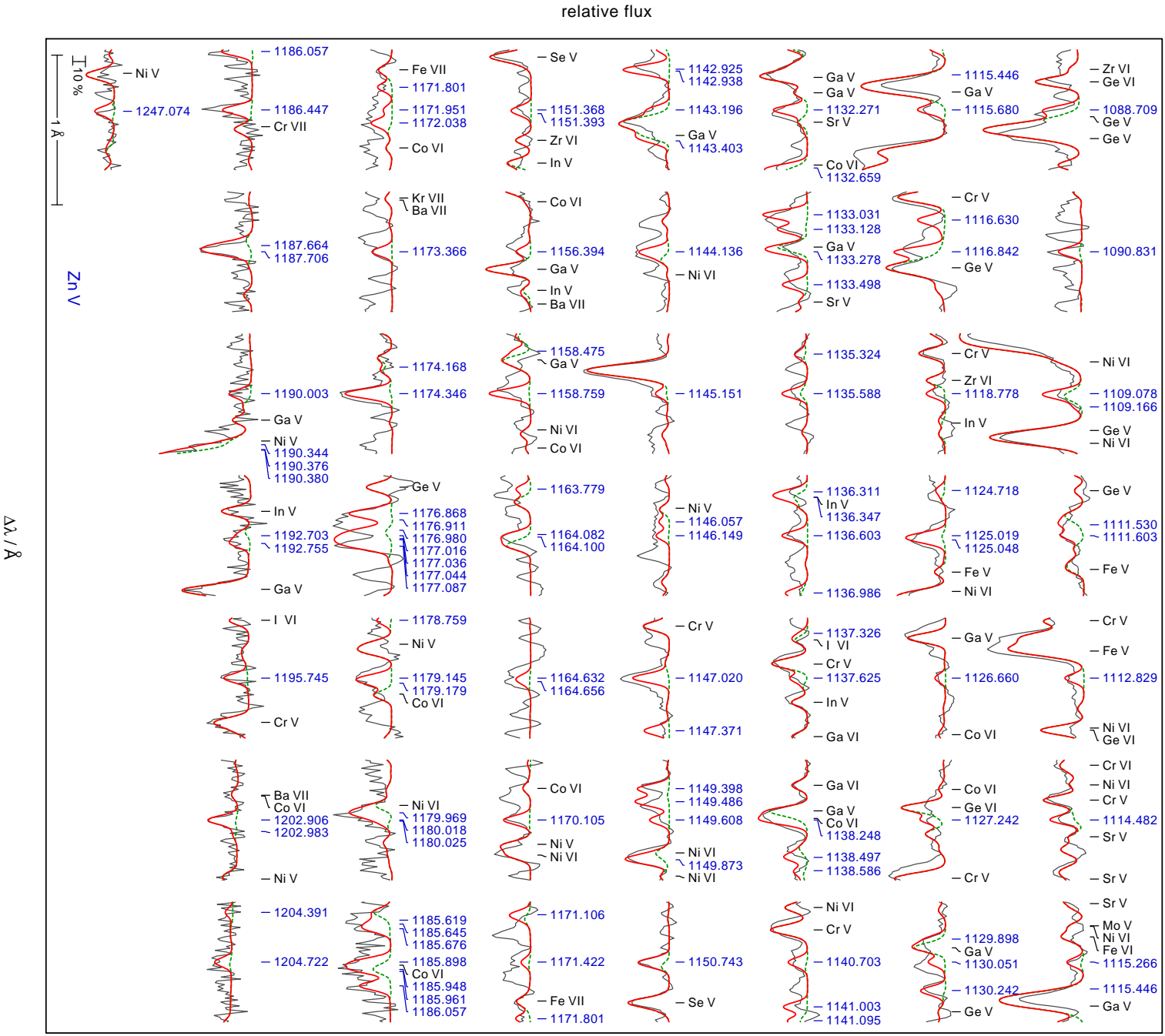


Figure B2. Prominent computed and identified lines of Zn V (blue wavelength labels) in the FUSE ($\lambda < 1180$ Å) and STIS observations of BD-22°3467. The model was calculated with the abundances given in Table A1 (red). In addition, a model without Zn (green dashed) is shown.

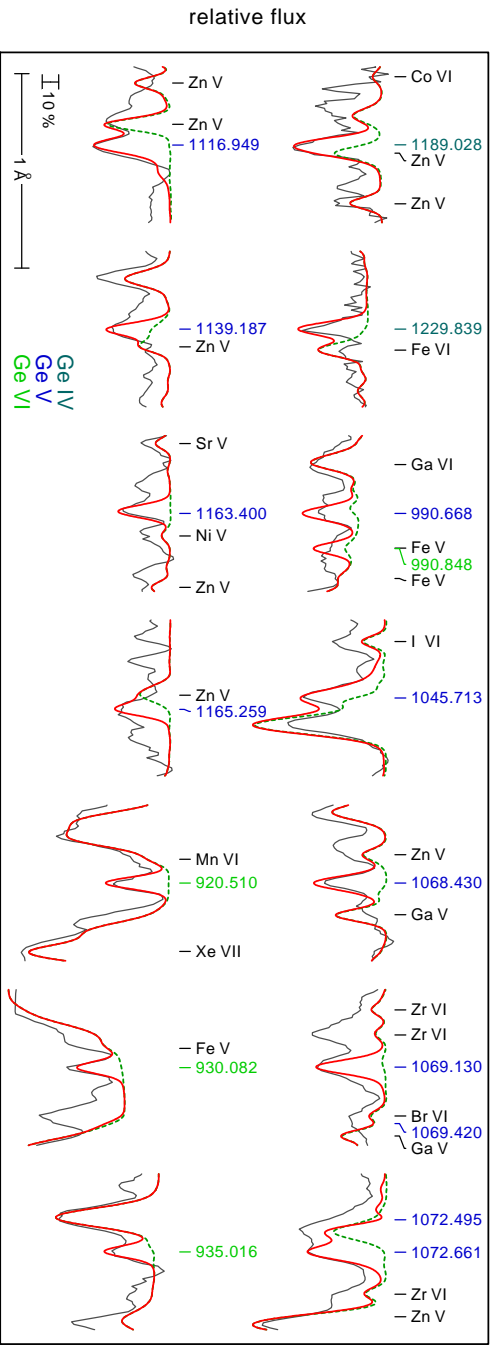


Figure B4. Like Fig. B2, for Ge IV (dark cyan), Ge V (blue), and Ge VI (green).

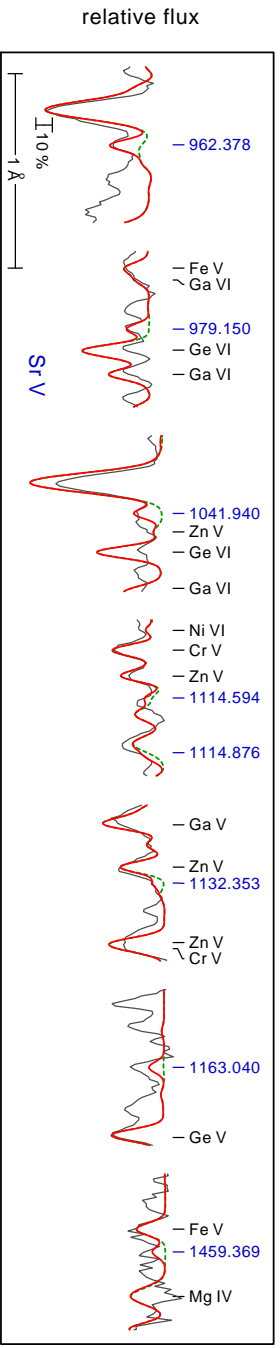


Figure B5. Like Fig. B2, for Sr V (blue).

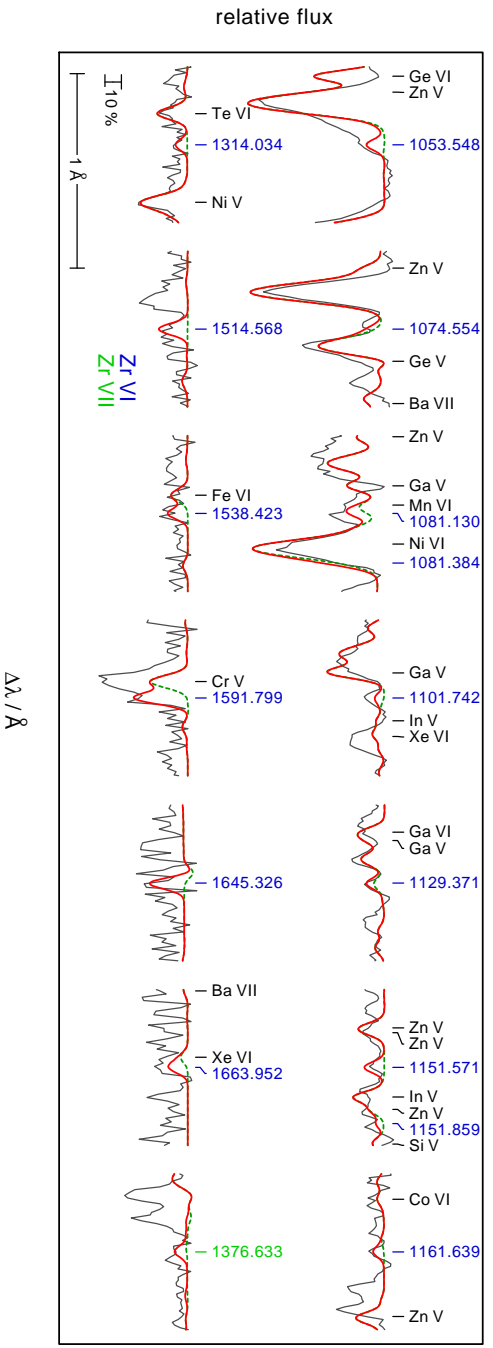


Figure B6. Like Fig. B2, for Zr VI (blue) and Zr VII (green).

Table B3: Cu lines with $W_\lambda \geq 5 \text{ m}\text{\AA}$ in the model spectrum of BD-22°3467.

Ion	Stage	Wavelength / \AA	Comment
Cu	VI	1060.890	too strong in the model
		1082.265	too weak in model
		1094.708	uncertain
		1098.480	uncertain
		1104.996	blend Ga v
		1115.821	uncertain
		1157.930	uncertain

Table B4: Identified Zn lines with $W_\lambda \geq 5 \text{ m}\text{\AA}$ in model spectrum of BD-22°3467.

Ion		Wavelength / \AA	Comment
Zn	IV	1239.119	
		1281.296	
Zn	V	1017.935	blend ISM
		1023.521	blend ISM
		1043.353	
		1052.441	blend ISM
		1053.278	blend ISM
		1055.878	blend ISM
		1056.330	uncertain
		1058.185	blend Ga v
		1061.472	uncertain
		1061.656	blend ISM
		1063.209	blend ISM
		1063.979	
		1066.547	uncertain
		1068.284	
		1069.674	uncertain
		1069.764	uncertain
		1071.501	blend ISM
		1072.992	blend ISM
		1074.241	uncertain
		1075.171	too strong in model
		1076.878	
		1085.290	uncertain
		1086.033	blend Ge v
		1086.739	blend ISM
		1088.709	
		1090.831	
		1094.088	blend ISM
1095.797	uncertain		
1095.961	uncertain		
1098.108			
1102.490	uncertain		
1103.598	too weak in model		
1104.199	blend ISM		
1106.788			
1107.318			
1109.078			
1109.166			
1111.530			
1111.603			
1112.829			

Table B4: continued.

Ion	Wavelength / Å	Comment
	1114.482	
	1115.266	
	1115.680	
	1116.630	too strong in model
	1116.842	
	1117.466	too weak in the model
	1118.778	
	1119.950	
	1120.101	uncertain
	1120.325	
	1121.109	blend Cr v, Fe vi
	1121.524	uncertain
	1122.502	blend ISM
	1123.127	blend Ga v
	1124.718	
	1125.019 1125.048	
	1126.660	
	1127.242	
	1128.098	blend Ga v
	1128.244	uncertain
	1128.813	
	1129.898	
	1130.051	
	1130.242	
	1131.242	
	1131.788	
	1132.271	
	1132.659	blend Co vi
	1133.031	
	1133.128	
	1133.278	
	1133.498	
	1135.324	
	1135.588	
	1136.311	
	1136.603	
	1136.986	
	1137.625	
	1138.248	blend Co vi
	1138.497	
	1138.586	
	1139.278	uncertain
	1139.997	uncertain
	1140.703	
	1141.003	
	1141.095	
	1141.344	uncertain
	1142.792	
	1142.925	
	1143.196	
	1143.403	blend Ga v
	1144.136	
	1145.151	
	1146.057	
	1146.149	
	1147.020	
	1147.371	
	1147.648	

Table B4: continued.

Ion	Wavelength / Å	Comment
	1148.922	
	1149.398	
	1149.486	
	1149.608	
	1149.873	blend Ni VI
	1150.743	
	1151.368	
	1151.787	uncertain
	1152.985	
	1153.160	
	1155.027	blend Fe VII
	1155.725	
	1156.394	
	1157.725	uncertain
	1158.475	blend Ga V
	1158.759	
	1160.221	
	1160.827	uncertain
	1161.971	
	1162.281	
	1162.401	uncertain
	1163.779	uncertain
	1164.090	
	1164.632	
	1165.189	blend Ge V
	1165.706	
	1165.880	too strong in model
	1168.302	uncertain
	1169.200	uncertain
	1169.301	uncertain
	1170.105	
	1170.885	uncertain
	1171.106	uncertain
	1171.422	
	1171.801	
	1171.951	
	1172.038	
	1173.366	
	1173.823	uncertain
	1173.892	too strong in model
	1174.346	
	1174.945	uncertain
	1176.122	
	1176.527	too weak in model
	1176.868 1176.911	
	1176.980 1177.016 1177.036 1177.087	
	1178.639	
	1178.759	
	1179.145	
	1179.969 1180.018	
	1182.019	uncertain
	1182.567	
	1183.041 1183.158	
	1183.314	uncertain
	1185.619 1185.645 1185.676	
	1185.898 1185.948 1185.961	
	1186.057	
	1186.447	

Table B4: continued.

Ion	Wavelength / Å	Comment
	1187.706	
	1189.072	
	1189.331	
	1190.003	
	1190.376	
	1192.014	
	1192.703 1192.755	
	1193.846	
	1195.745	
	1198.795	
	1200.639	
	1201.961	
	1202.128	too strong in model
	1202.906	
	1204.391	
	1204.722	
	1205.380	too strong in the model
	1224.788	
	1230.267	
	1238.430	
	1239.108	
	1247.065	
	1262.252	
	1268.158	
	1274.197	
	1281.310	
	1295.850	too strong in model
	1302.786	
	1318.204	
	1344.241	too strong in model

Table B5: Like Table B4, for Ga.

Ion	Wavelength / Å	Comment	
Ga	IV	965.237 965.272	blend ISM
		981.831	blend ISM
		1003.780	blend ISM
		1004.367	
		1005.270	
		1009.849	blend ISM
		1010.080	blend ISM
		1014.822	uncertain
		1074.966	uncertain
Ga	V	943.583	
		962.084	uncertain
		967.324 967.404	blend Ge VI
		979.614	
		980.988	
		982.395	blend ISM
		984.078	
		990.138	uncertain
		997.855	blend ISM
		1002.617	blend ISM
		1009.928	blend ISM
		1014.456	blend ISM
		1014.868	uncertain

Table B5: continued.

Ion	Wavelength / Å	Comment
	1015.610	too strong in model
	1019.711	uncertain
	1032.375	blend ISM
	1033.492 1033.549 1033.580	
	1034.822	
	1037.334	blend ISM
	1038.778	blend ISM
	1040.204	blend ISM
	1045.850	blend ISM
	1047.504	
	1050.453	
	1053.930	blend ISM
	1054.430	uncertain
	1054.563	blend Ge v
	1058.123	
	1062.677	
	1063.807	blend ISM
	1065.371	uncertain
	1068.593 1068.616	too strong in model
	1069.484 1069.530	too strong in model
	1069.587	too strong in model
	1071.123 1071.168	
	1073.791	
	1074.911	uncertain
	1078.225	blend ISM
	1078.795	
	1079.587 1079.599	
	1079.879 1079.925	
	1080.474	blend ISM
	1080.988	uncertain
	1087.358	
	1088.068	
	1091.703	
	1094.355	blend ISM
	1094.739	
	1095.110	
	1100.401	uncertain
	1101.613	uncertain
	1102.767 1102.803	too strong in model
	1103.047	too strong in model
	1104.936	
	1105.253	
	1105.620	
	1107.763	
	1109.829	blend ISM
	1115.561	blend ISM
	1118.018	
	1118.318	
	1120.260	blend ISM
	1123.154	
	1123.646	
	1126.393	
	1127.332	
	1127.726	
	1127.752	
	1128.082	blend Zn v
	1128.554	
	1129.152	

Table B5: continued.

Ion	Wavelength / Å	Comment
	1129.956	
	1131.452	
	1132.054	
	1132.157	
	1133.247	blend Zn v
	1133.903	
	1136.067	
	1138.187	
	1143.367	
	1145.974	
	1148.409	too strong in model
	1150.113	
	1150.219	
	1154.708	uncertain
	1155.976	
	1156.511	
	1157.729	uncertain
	1158.534	
	1160.847	uncertain
	1161.994	uncertain
	1162.048	uncertain
	1178.967	blend Ni v
	1180.958	uncertain
	1183.110	
	1183.656	
	1189.329	blend Zn v
	1190.179	uncertain
	1191.029	
	1193.061	
	1197.633	
	1265.454	
	1276.911	blend Fe vI
	1283.615	
	1311.389	
Ga	vI	no observation
	915.720	blend ISM
	919.117	blend ISM
	929.964	blend ISM
	935.522	blend ISM
	945.329	blend ISM
	948.171	blend ISM
	953.738	blend ISM
	955.510	blend ISM
	955.616	blend ISM
	956.648	blend ISM
	957.642	blend ISM
	960.172	blend ISM
	961.262	blend ISM
	964.264 964.311 964.363	blend ISM
	964.569 964.647	blend ISM
	964.831 964.925	blend ISM
	966.130	blend ISM
	966.255	blend ISM
	966.990	blend ISM
	967.825	blend ISM
	968.107	
	970.064	
	974.853	
	975.165	

Table B5: continued.

Ion	Wavelength / Å	Comment
	975.342 975.396	blend ISM
	976.133	blend ISM
	977.848	blend ISM
	978.897	uncertain
	979.298 979.383	
	979.689	
	980.240	too strong in model
	980.489	uncertain
	980.580	blend ISM
	982.066	blend ISM
	983.110 983.160	
	983.430 983.485	uncertain
	983.630	
	984.009	blend ISM
	985.273	
	985.596	blend ISM
	985.812	blend ISM
	986.662	blend ISM
	987.862	blend ISM
	988.063	blend ISM
	989.169	blend ISM
	989.374	
	990.416	blend ISM
	990.639	
	992.053	blend ISM
	992.709	blend ISM
	993.094	
	993.640 993.654	blend ISM
	994.051	blend ISM
	995.305	
	996.027	blend ISM
	996.309 996.391	uncertain
	996.556	
	997.605	blend ISM
	999.083	blend ISM
	999.673	
	999.945	
	1000.117	
	1000.531	too strong in model
	1001.483	
	1001.821	blend ISM
	1002.376	blend ISM
	1002.985	uncertain
	1003.127 1003.147	uncertain
	1003.390 1003.427	uncertain
	1003.691	uncertain
	1004.170	blend ISM
	1004.355	
	1005.228	uncertain
	1006.156	uncertain
	1006.396	blend ISM
	1006.894 1006.951	too strong in model
	1007.264	blend Fe v
	1007.511	blend Fe v
	1008.086	blend ISM
	1008.757	blend ISM
	1008.924 1009.049	blend ISM
	1009.262	

Table B5: continued.

Ion	Wavelength / Å	Comment
	1009.512	blend ISM
	1009.743 1009.796 1009.806	blend ISM
	1010.102	blend ISM
	1011.047	blend ISM
	1011.696 1011.698	blend ISM
	1012.260	blend ISM
	1013.620	blend ISM
	1014.434	blend ISM
	1015.598	too strong in model
	1015.782	
	1016.307	uncertain
	1017.003	
	1017.074	
	1018.785	
	1019.083	blend ISM
	1019.206	
	1020.741	blend ISM
	1022.008 1022.098	uncertain
	1027.809	uncertain
	1029.168	uncertain
	1030.457 1030.469	uncertain
	1037.061	blend ISM
	1037.419	blend ISM
	1038.800	blend ISM
	1042.324	blend Fe v
	1047.696	blend ISM
	1051.311	blend ISM
	1051.589	blend ISM
	1058.653	
	1058.931	
	1059.854 1058.931	
	1060.387	uncertain
	1061.790	blend ISM
	1063.972	uncertain
	1066.724	blend ISM
	1071.544	blend ISM
	1073.814	
	1076.760	
	1077.944	blend ISM
	1078.331	blend ISM
	1089.450	
	1099.109	
	1101.237	
	1105.669	
	1106.251	
	1121.262	uncertain
	1129.110	
	1138.016	
	1149.078	
	1237.472	
	1259.673	blend Co vi
	1288.359	

Table B6: Like Table B4, for Ge.

Ion	Wavelength / Å	Comment
Ge IV	936.765	blend ISM
	1189.028	
	1229.839	
Ge V	1494.889	uncertain
	942.717	blend ISM
	958.508	
	965.501	
	971.357	blend ISM
	977.455	
	984.923	blend ISM
	986.767	blend ISM
	988.132	blend ISM
	990.668	
	992.307	blend ISM
	1004.380	
	1004.938	too strong in model
	1008.122	blend ISM
	1016.667	
	1033.107	too strong in model
	1035.504	uncertain
	1038.430	
	1042.127	too strong in model
	1045.713	
	1048.318 1048.371 1048.411	uncertain
	1050.057	blend ISM
	1054.590	
1058.932		
1068.430		
1069.132		
1069.420	too strong in model	
1069.703		
1069.857	uncertain	
1072.495		
1072.659		
1080.427 1080.484 1080.586	blend ISM	
1086.653		
1087.855		
1089.491 1089.526		
1092.089		
1103.185	uncertain	
1116.947		
1123.746	too strong in model	
1125.424		
1139.187		
1163.400		
1165.259		
1176.690	uncertain	
1222.300		
Ge VI	911.098	no observation
	911.114	no observation
	914.143	no observation
	915.041	no observation
	917.352	blend ISM
	918.280	blend ISM
	919.278	blend ISM
	919.731 919.760	blend ISM
	920.510	

Table B6: continued.

Ion	Wavelength / Å	Comment
	921.084	blend ISM
	921.780	blend ISM
	923.486	uncertain
	925.476	
	926.822	too strong in model
	928.136	
	928.907	
	929.428	blend ISM
	929.631	blend ISM
	930.081	
	933.766	blend ISM
	935.016	
	935.912	
	939.152	blend ISM
	940.427	
	942.474	blend ISM
	942.567	blend ISM
	944.851	blend ISM
	946.589	blend ISM
	947.937	
	951.739	
	952.415	blend ISM
	953.132	
	954.504	blend ISM
	955.708	blend ISM
	957.548	blend ISM
	957.886	
	958.100	
	958.310	uncertain
	960.102	too strong in model
	964.813	blend ISM
	965.203	blend ISM
	965.914	blend ISM
	967.300	
	968.723	
	969.010	blend ISM
	969.171	blend ISM
	969.568	
	970.977	blend ISM
	971.392	blend ISM
	973.353	blend ISM
	975.996	
	979.258	
	979.905	blend ISM
	980.431	blend ISM
	980.697	too strong in model
	981.946	blend ISM
	983.648	
	988.180	too strong in model
	990.049	blend ISM
	990.848	blend Fe v
	991.519	blend ISM
	991.888	blend ISM
	992.377	blend He II
	993.015	blend ISM
	995.289	
	996.771	too strong in model
	1002.276	blend ISM

Table B6: continued.

Ion	Wavelength / Å	Comment
	1004.661	
	1008.410	blend ISM
	1011.518	
	1013.528	blend ISM
	1014.766	
	1015.582	too strong in model
	1016.817	blend ISM
	1023.527	blend ISM
	1031.263 1031.324	blend ISM
	1033.152	too strong in model
	1034.251	uncertain
	1039.483	too strong in model
	1039.890	too strong in model
	1047.139	too strong in model
	1047.207	too strong in model
	1051.515	blend ISM
	1053.196	too strong in model
	1061.890	
	1062.394	
	1064.323	
	1080.148	too strong in model
	1080.510	blend ISM
	1088.522	
	1102.998	too strong in model
	1103.103	too strong in model
	1106.146	too strong in model
	1113.177	
	1121.431	uncertain
	1127.159	
	1148.327	too strong in model
	1227.850	too strong in model
	1228.870	too strong in model
	1237.128	
	1237.892	too strong in model
	1251.447	too strong in model
	1255.318	
	1257.218	blend Mo v
	1292.751	too strong in model
	1300.093	too strong in model
	1305.406	too strong in model
	1391.639	too strong in model
	1500.600	

Table B7: Like Table B4, for Se.

Ion	Wavelength / Å	Comment
Se v	943.957	blend ISM
	964.515	blend ISM
	1030.609	
	1047.219	too strong in model
	1059.951	uncertain
	1094.691	
	1151.016	
	1184.343	
	1227.540	
	1249.048	uncertain

Table B7: continued.

Ion	Wavelength / Å	Comment
	1264.063	blend Mn vi
	1426.676	
	1433.568	
	1445.567	
	1447.283	
	1447.408	
	1451.653	
	1454.292	
	1473.253	
	1730.014	
	1736.835	no observation
	1740.038	no observation

Table B8: Like Table B4, for Br.

Ion	Wavelength / Å	Comment
Br v	945.815	blend ISM
	1069.410	
Br vi	955.883	blend ISM
	966.753	blend ISM
	969.735	blend ISM
	981.423	
	1050.548	
	1069.382 1069.432	uncertain
	1073.708	
	1074.992	
	1230.318	
	1399.153	

Table B9: Like Table B4, for Kr.

Ion	Wavelength / Å	Comment
Kr vi	927.334	blend ISM
	944.046	uncertain
	965.093	blend ISM
	980.411	uncertain
	1002.748	
	1045.238	
Kr vii	1061.064	blend ISM
	918.444	
	960.645	
	1197.166	
	1197.166	

Table B10: Like Table B4, for Sr.

Ion	Wavelength / Å	Comment
Sr v	917.802	blend ISM
	927.356	blend ISM
	928.353	blend ISM
	935.509	blend ISM

Table B10: continued.

Ion	Wavelength / Å	Comment
	936.808	blend ISM
	942.943	blend ISM
	946.530	blend ISM
	951.044	blend ISM
	951.159	blend ISM
	955.369	blend N iv
	957.714	blend ISM
	962.378	
	969.103	blend ISM
	979.150	
	985.408	blend ISM
	1007.201	uncertain
	1011.422	
	1013.714	blend ISM
	1020.002	uncertain
	1020.439	
	1030.445	too strong in model
	1031.343	blend ISM
	1038.990	uncertain
	1041.940	
	1056.104	uncertain
	1065.215	uncertain
	1070.578	uncertain
	1114.594	
	1114.876	uncertain
	1132.353	uncertain
	1141.221	uncertain
	1152.104	uncertain
	1154.871	
	1163.040	
	1164.173	blend Zn v
	1175.115	uncertain
	1200.728	blend ISM
	1238.652	blend Ni v
	1280.995	
	1281.911	
	1311.334	
	1311.781	blend Fe v
	1387.288	
	1415.404	
	1447.665	
	1459.369	
	1472.784	
Sr	vi 912.3760	no observation

Table B11: Like Table B4, for Zr.

Ion	Wavelength / Å	Comment
Zr	v 1200.802	blend ISM
	1332.065	
Zr	vi 955.500	
	1040.904	
	1040.995	
	1044.483	uncertain
	1050.580	blend Br vi
	1053.548	

Table B11: continued.

Ion	Wavelength / \AA	Comment
	1064.818	blend ISM
	1068.836	
	1072.877	
	1073.197	uncertain
	1074.554	
	1081.130	
	1081.384	blend ISM
	1088.439	uncertain
	1095.491	
	1099.591	
	1101.742	
	1108.491	blend ISM
	1113.736	uncertain
	1114.481	
	1118.689	too strong in model
	1129.371	
	1134.606	uncertain
	1142.550	
	1143.933	
	1150.774	
	1151.571	
	1158.582	uncertain
	1161.639	
	1314.034	
	1417.865	
	1514.568	
	1521.699	
	1529.396	
	1536.035	uncertain
	1538.423	
	1541.255	uncertain
	1591.799	
	1604.549	uncertain
	1645.326	
	1663.952	
	1679.018	uncertain
	1682.241	
	1683.302	uncertain
	1733.091	no observation
	1733.937	no observation
	1741.948	no observation
	1749.350	no observation
Zr VII	1233.578	
	1234.964	
	1376.633	
	1469.098	uncertain

Table B12: Like Table B4, for Mo.

Ion	Wavelength / \AA	Comment
Mo VI	995.806	uncertain
	1038.640	blend ISM
	1047.182	uncertain
	1479.168	
	1595.435	

Table B13: Like Table B4, for In.

Ion	Wavelength / Å	Comment
In v	933.577	blend ISM
	940.079	uncertain
	942.218	uncertain
	1101.860	uncertain
	1122.517	blend ISM
	1135.588	uncertain
	1136.347	
	1137.787	
	1148.852	
	1151.723	
	1153.836	
	1156.652	
	1160.561	
	1168.056	
	1177.447	
	1181.329	
	1183.049	
	1190.489	blend ISM
	1191.583	
	1192.278	
	1192.541	
	1196.281	
	1199.170	
	1200.843	blend ISM
	1210.126	uncertain
	1228.000	uncertain
	1228.483	uncertain
	1238.448	
	1241.025	
	1241.299	
	1242.210	
	1243.632	blend Ni v
	1252.836	blend Fe vi
1256.570	uncertain	
1276.318	uncertain	
1278.758		
1285.468	uncertain	
1289.800		
1290.449		
1292.930		
1295.035	uncertain	
1296.427		
1315.139		
1317.671	uncertain	
1320.468	uncertain	
1334.123		
1339.599		
1355.458	uncertain	

Table B14: Like Table B4, for Te.

Ion	Wavelength / Å	Comment
Te vi	951.021	blend ISM
	1071.414	
	1242.023	uncertain

Table B14: continued.

Ion	Wavelength / \AA	Comment
	1267.986	
	1313.874	

Table B15: Like Table B4, for I.

Ion	Wavelength / \AA	Comment
I VI	911.192	no observation
	919.210	blend ISM
	970.448	uncertain
	987.381	blend ISM
	989.005	blend ISM
	1000.999	uncertain
	1045.423	
	1053.389	blend ISM
	1057.530	
	1120.301	blend ISM
	1121.218	uncertain
	1137.370	uncertain
	1153.262	too strong in model
	1185.111	uncertain
	1191.601	
	1195.359	uncertain
	1395.979	

Table B16: Like Table B4, for Xe.

Ion	Wavelength / \AA	Comment
Xe VI	1080.080	blend Ge VI
	1091.630	uncertain
	1136.410	uncertain
Xe VII	912.875	no observation
	920.861	blend ISM
	942.152	
	943.218	
	970.177	uncertain
	995.510	
	997.407	blend Fe V
	1071.226	uncertain
	1077.110	blend ISM
	1093.781	blend ISM
	1243.565	
	1460.856	uncertain

Table B17: Like Table B4, for Ba.

Ion	Wavelength / \AA	Comment
Ba VI	937.595	blend ISM
Ba VII	924.898	blend ISM
	943.102	blend ISM
	993.411	

Table B17: continued.

Ion	Wavelength / Å	Comment
	1074.937	
	1255.520	uncertain
	1465.045	
Ba VIII	921.761	uncertain
	941.168	uncertain
	952.762	blend ISM
	961.679	blend ISM
	1013.130	blend ISM
	1039.555	
	1048.339	blend ISM
	1074.911	
	1083.072	
	1113.140	uncertain

This paper has been typeset from a \TeX/L\AA\TeX file prepared by the author.